COMPRESSIBLE SLIP FLOW THROUGH CONSTRICTED CYLINDERS WITH DENSITY-DEPENDENT VISCOSITY

Katrin Rohlf

Department of Mathematics
Ryerson University
350 Victoria St.
Toronto, Ontario, M5B 2K3, Canada

Abstract. A second-order non-linear differential equation for pressure/density is derived for a weakly compressible fluid with density-dependent viscosity and slip, through a local constriction. Solution curves are presented for scaled pressure/density curves, for scaled pressure/density gradient, and for the scaled centerline velocity. The effect of the viscosity-density parameter is explored for large vessels where compressibility and slip values are relatively small, and for small vessels where compressibility and slip effects can be more substantial. Results for solution curves for large vessels have physiological relevance to blood flows, while small vessel results apply to particle-based numerical simulations with applications to microchannel flows.

Keywords. pressure, gradient, compressible, constriction, slip, Karman-Pohlhausen method, viscosity-density dependence

AMS (MOS) subject classification: 65L06, 76M28, 76N99, 76Z05, 92C35.

1 Introduction

Understanding the properties of flows through a local constriction is physiologically relevant for blood flow applications [1, 2, 3, 4, 5, 6, 7, 8], as well as for flows through microfluidic devices [9, 10, 11]. In the former application, blood is typically modeled as an incompressible or weakly compressible viscous fluid, with either small [12, 13, 14, 6, 15, 16, 17, 18] or — more commonly — no slip at the wall [1, 2, 3, 4, 5, 7, 8]. Constrictions represent pathological flow conditions connected to atherosclerotic plaques (flow through stenosis), and studies of this type can help identify physiologically vulnerable states (potential vessel rupture), as well as provide insight to treatment options. Reynolds numbers are typically high for blood flow applications compared to microfluid flow. In microfluidic devices, Reynolds numbers are much smaller and the effect of compressibility and slip on flows through constrictions becomes an important aspect of study. Additionally, particle-based

methods used to simulate either flow application [19, 20, 16, 17, 21], have built-in compressibility, and, in the case of multiparticle collision dynamics (MPCD), which is a popular particle-based method, the viscosity depends on density [22]. Other compressible flows with density/pressure-dependent viscosity include microfluidic flows, flows for polymer and food processing, pumping of crude oil and fuel oil, and some geophysical flows [23, 24, 25, 26].

Theoretical work on flow through a local constriction was pioneered in the work of [5, 27], using the Karman-Pohlhausen method. The velocity profile, as well as pressure curves, were derived for an incompressible Newtonian fluid through a constricted cylinder subject to the no-slip assumption, and compared to experimental results. All nonlinear terms involving the pressure gradient, as well as second-order derivative pressure terms, were dropped. In [28], a third-order polynomial expression was used for the velocity to derive pressure and pressure gradient curves. Quadratic pressure gradient terms were retained in the derivation. Incorporating compressibility and slip, [16] derived velocity and pressure curves, again dropping non-linear pressure gradient and second-order pressure derivative terms. Recently Rabba and Rohlf [29] provided pressure and pressure gradient curves retaining all nonlinear and second-order derivative terms, incorporating slip and compressibility. All of these studies were for Newtonian fluids with constant viscosity, although the Karman-Pohlhausen method has also been used to study a micropolar fluid [30], a couple stress fluid [31], and a power law fluid [32].

In this paper, theoretical pressure, pressure gradient, and centerline velocity curves are presented for force-driven, weakly compressible Newtonian fluids with density-dependent viscosity, through mild constrictions subject to small slip at the wall. A fourth-order polynomial expression is used for the velocity, and all non-linear pressure gradient terms, as well as second-order derivative terms, are retained in the analysis. Results for large Reynolds number flows are presented, so as to connect the results to blood flow applications. Additionally, the resulting density/pressure and centerline velocity curves are compared to numerical multi-particle collision dynamics flow solutions so as to test the model for small Reynolds number flows, where the viscosity-density relationship is known to satisfy the linear relationship used in this analysis.

The paper is organized as follows: Section 2 provides the governing equations of motion that are approximated in Section 3 to derive the differential equation governing the density/pressure using the Karman-Pohlhausen method. Section 4 provides some important upstream relationships and the flow geometries necessary for solving the differential equation numerically. The next section 5 presents numerical solution curves for both large vessels (blood flow applications), and for smaller ones (multiparticle collision dynamics flows and microchannels). Section 6 provides a discussion of the results, including a phase-plane analysis for the first-order system that was used to solve the non-linear second-order pressure/density ODE from Section 3 numerically. The last Section 7 provides a summary and conclusions

of the results.

2   Governing Equations

The governing equations of motion for a forced, steady, compressible Newtonian fluid with variable viscosity [33, 34] are

$$\rho \, (\mathbf{u} \cdot \nabla)\mathbf{u} \;=\; -\nabla P + \nabla \cdot \boldsymbol{\tau} + \mathbf{F} \tag{1}$$

$$\boldsymbol{\tau} \;=\; \mu \left(\nabla \mathbf{u} + \nabla \mathbf{u}^T \right) - \frac{2}{3}\mu(\nabla \cdot \mathbf{u})\mathbf{I} \tag{2}$$

$$\nabla \cdot (\rho \mathbf{u}) \;=\; 0 \tag{3}$$

where ρ is the density, P is the pressure, μ is the variable viscosity, $\mathbf{u}$ is the velocity vector, $\mathbf{F}$ is the external force, $\boldsymbol{\tau}$ is the shear stress tensor and $\mathbf{I}$ is the identity tensor. Additionally, ∇ is the gradient operator for the spatial coordinates x, y and z, and it is assumed that the coefficient of bulk viscosity κ is negligible. Many fluids satisfy the Stokes assumption (negligible bulk viscosity), including multi-particle collision dynamics flows [35].

The pressure-density and viscosity-density relationships, are taken to be linear, namely

$$P \;=\; P_0 + \frac{k_B T}{m}(\rho - \rho_0), \tag{4}$$

$$\mu \;=\; \mu_0 \left(1 + A \frac{\rho}{\rho_0} \right). \tag{5}$$

Here k_B is the Boltzmann constant, T is the constant system temperature, m is the mass of a fluid particle, A is a viscosity-density parameter, and P_0, ρ_0, and μ_0 are the constant reference pressure, density, and viscosity, respectively. Equation (4) represents an ideal gas equation of state, and (5) has been shown to be valid for a range of densities ρ for multiparticle collision (MPC) dynamics simulations (see Appendix C of [22]). Generalized linear equations of state, including the ideal gas equation of state, are also needed to model certain flows, including microfluidics and some geophysical flows [22, 36].

Assuming the flow is axisymmetric with forcing in the axial z direction (eg. $\mathbf{F} = (0, 0, \rho g)$, g an acceleration constant), the equations can be written in cylindrical coordinates with assumed velocity vector

$$\mathbf{u} = (u_r, u_\theta, u_z) = (u(r, z), 0, w(r, z)), \tag{6}$$

where r is the radial coordinate, together with $\rho = \rho(r, z)$ and $P = P(r, z)$.

In this case, the governing equations of motion become

$$\frac{\partial}{\partial r}(\rho u) + \frac{\partial}{\partial z}(\rho w) + \frac{\rho u}{r} \;=\; 0 \qquad\qquad \text{(mass)} \tag{7}$$

$$\rho \left(u\frac{\partial u}{\partial r} + w\frac{\partial u}{\partial z} \right) = -\frac{\partial P}{\partial r} \qquad (r\text{-momentum}) \qquad (8)$$

$$+ \mu \left(\frac{\partial^2 u}{\partial r^2} + \frac{1}{r}\frac{\partial u}{\partial r} + \frac{\partial^2 u}{\partial z^2} - \frac{u}{r^2} \right) + \frac{\mu}{3}\frac{\partial}{\partial r}(\nabla \cdot \mathbf{u})$$

$$+ 2\frac{\partial \mu}{\partial r}\frac{\partial u}{\partial r} - \frac{2}{3}(\nabla \cdot \mathbf{u})\frac{\partial \mu}{\partial r} + \frac{\partial \mu}{\partial z}\left(\frac{\partial w}{\partial r} + \frac{\partial u}{\partial z} \right)$$

$$\rho \left(u\frac{\partial w}{\partial r} + w\frac{\partial w}{\partial z} \right) = \rho g - \frac{\partial P}{\partial z} \qquad (z\text{-momentum}) \qquad (9)$$

$$+ \mu \left(\frac{\partial^2 w}{\partial r^2} + \frac{1}{r}\frac{\partial w}{\partial r} + \frac{\partial^2 w}{\partial z^2} \right) + \frac{\mu}{3}\frac{\partial}{\partial z}(\nabla \cdot \mathbf{u})$$

$$+ 2\frac{\partial \mu}{\partial z}\frac{\partial w}{\partial z} - \frac{2}{3}(\nabla \cdot \mathbf{u})\frac{\partial \mu}{\partial z} + \frac{\partial \mu}{\partial r}\left(\frac{\partial w}{\partial r} + \frac{\partial u}{\partial z} \right)$$

$$P(r,z) = P_0 + \frac{k_B T}{m}(\rho(r,z) - \rho_0) \qquad (\text{equation of state}) \qquad (10)$$

$$\mu(r,z) = \mu_0 \left(1 + A\,\frac{\rho(r,z)}{\rho_0} \right) \qquad (\text{viscosity equation}) \quad (11)$$

where

$$\nabla \cdot \mathbf{u} = \frac{u}{r} + \frac{\partial u}{\partial r} + \frac{\partial w}{\partial z}. \qquad (12)$$

With the forcing in the z direction only, the θ-momentum equation is identically satisfied.

3 Differential equation for pressure/density

The derivation of the pressure/density differential equation (DE) follows the same steps and assumptions as outlined in [29]. As such, only the essential steps are highlighted here.

Note that due to the equation of state (10), one can easily switch between density and pressure in the resulting DE. Typically large vessel discussions focus on pressure and pressure gradient curves, while flows described by particle-based methods generally focus on densities.

3.1 Integrated z-momentum equation

First, the z-momentum equation is integrated using conservation of mass and the slip boundary condition

$$\mathbf{u} \cdot \mathbf{t} = w_s, \quad \text{and} \quad \mathbf{u} \cdot \mathbf{n} = 0, \qquad (13)$$

where $\mathbf{t}$ and $\mathbf{n}$ are the unit tangent and normal directions at a given point on the constricted cylinder wall.

Considering mild constrictions described by a radius $R = R(z)$, for which $P = P(z)$, it follows that $\rho = \rho(z)$ from the equation of state, and hence

$\mu = \mu(z)$ from the viscosity-density relationship. The conservation of mass equation then gives

$$\frac{\partial u}{\partial r} + \frac{u}{r} = -\frac{1}{\rho}\frac{\partial}{\partial z}(\rho w), \tag{14}$$

which can be substituted in the z-momentum equation, the z-momentum equation can then be integrated, and various applications of the Leibniz rule, use of constant flow rate

$$Q = \pi\rho R^2 \overline{W} = 2\pi\rho \int_0^R rw(r,z)dr, \tag{15}$$

and other straight-forward simplifications (see [29]), lead to the integrated z-momentum equation

$$\begin{aligned}
\frac{1}{2}\frac{d}{dz}\int_0^R rw^2 dr = {} & -\frac{1}{2}\frac{RR'w_s^2}{(1+R'^2)} - \frac{1}{\rho}\frac{dP}{dz}\frac{R^2}{2} \\
& + \frac{1}{\rho}\,\mu_0\left(1+A\frac{\rho}{\rho_0}\right)\left[R\left(\frac{\partial w}{\partial r}\right)\bigg|_{r=R} + \frac{4}{3}\frac{d^2}{dz^2}\int_0^R rwdr\right] \\
& - \frac{4}{3}\frac{1}{\rho}\,\mu_0\left(1+A\frac{\rho}{\rho_0}\right)\left[\frac{Rw_s R''}{\sqrt{1+R'^2}} + \frac{w_s R'^2}{\sqrt{1+R'^2}}\right] \\
& + \frac{1}{3\rho^2}\mu_0\left(1+A\frac{\rho}{\rho_0}\right)\left[\frac{\rho(RR''+R'^2)}{\sqrt{1+R'^2}}w_s + \frac{2Rw_s R'}{\sqrt{1+R'^2}}\frac{m}{k_B T}\frac{dP}{dz}\right] \\
& - \frac{1}{3\rho^2}\mu_0\left(1+A\frac{\rho}{\rho_0}\right)\left[\frac{2R\rho w_s R'^2 R''}{(1+R'^2)^{3/2}}\right] + \frac{gR^2}{2} \\
& + \frac{8}{3}\frac{\mu_0}{\rho}\left(1+A\frac{\rho}{\rho_0}\right)\frac{RR'^2 R''w_s}{(1+R'^2)^{3/2}} - \frac{\mu_0}{3\rho^2}\left(1+A\frac{\rho}{\rho_0}\right)\frac{m}{k_B T}\frac{dP}{dz}\frac{Rw_s R'}{\sqrt{1+R'^2}} \\
& - \frac{2}{\rho}\frac{\mu_0 A}{\rho_0}\frac{m}{k_B T}\frac{dP}{dz}\left[\frac{Rw_s R'}{\sqrt{1+R'^2}} + \frac{m}{k_B T}\frac{1}{3\rho}\frac{dP}{dz}\int_0^R rwdr\right].
\end{aligned} \tag{16}$$

Note that through the ideal gas equation of state, one can write all density terms as pressure terms or vice versa.

In (16), except for the integral on the left-hand-side and for $\left(\frac{\partial w}{\partial r}\right)\big|_{r=R}$, all terms are either known flow parameters (μ_0, A, ρ_0, w_s, $k_B T/m$, flow rate Q given in (15)), based on the known flow geometry (R, R', R''), or for the unknown pressure or density (P or ρ) that is to be solved for.

The Karman-Pohlhausen method is used to approximate the unknown w terms (the integral on the left-hand-side, and $\left(\frac{\partial w}{\partial r}\right)\big|_{r=R}$) in terms of the pressure gradient, after which point the differential equation for pressure/density is obtained.

3.2 Karman-Pohlhausen method

As per the pioneering work of [5], and subsequent studies including ([29, 16, 28]), the axial velocity w is taken to be a function of the scaled radial coordinate $\eta = \frac{R-r}{R}$, whose value is zero at the wall, and one at the center of the vessel. The specific form is taken to be

$$\frac{w(r,z)}{W} = A\eta + B\eta^2 + C\eta^3 + D\eta^4 + E, \tag{17}$$

where

$$A = \frac{1}{7}\left(-\lambda + 10 - 12E + T + 2\frac{w_s}{W}\right) \tag{18}$$

$$B = \frac{1}{7}\left(3\lambda + 5 - 6E - 3T + \frac{w_s}{W}\right) \tag{19}$$

$$C = \frac{1}{7}\left(-3\lambda - 12 + 20E + 3T - 8\frac{w_s}{W}\right) \tag{20}$$

$$D = \frac{1}{7}\left(\lambda + 4 - 9E - T + 5\frac{w_s}{W}\right) \tag{21}$$

$$E = \frac{w_s}{W\sqrt{1+R'^2}}. \tag{22}$$

The expressions for A-E are found by imposing

(i) $w = \dfrac{w_s}{\sqrt{1+R'^2}}$ at $r = R$ (slip boundary condition)

(ii) $\dfrac{\partial w}{\partial r} = 0$ at $r = 0$ (axisymmetric flow)

(iii) $w = W$ at $r = 0$ (definition of centerline velocity),

(iv) $\dfrac{\partial^2 w}{\partial r^2} = -\dfrac{2(W - w_s)}{R^2}$ at $r = 0$ (nearly parabolic flow with slip),

(v) $\dfrac{dP}{dz} \approx \rho g + \mu\left(\dfrac{\partial^2 w}{\partial r^2} + \dfrac{1}{r}\dfrac{\partial w}{\partial r}\right)$ at $r = R$ (from z-mom equation).

Here, w_s is magnitude of the velocity vector at $r = R$ (see (13), and

$$\lambda = \frac{R^2}{\mu W}\frac{dP}{dz} \quad \text{and} \quad T = \frac{\rho g R^2}{\mu W}. \tag{23}$$

The centerline velocity W, which is as yet an unknown function of the axial coordinate z, can be shown to satisfy

$$W = \frac{2}{97}\frac{R^2}{\mu}\frac{dP}{dz} + \frac{210}{97}\overline{W} - \frac{102}{97}\frac{w_s}{\sqrt{1+R'^2}} - \frac{2}{97}\frac{\rho g R^2}{\mu} - \frac{11}{97}w_s \tag{24}$$

where $\overline{W}$ is the average velocity as per (15).

The axial velocity (17) is now used to evaluate the integral term on the left hand side of (16), as well as the $\left(\frac{\partial w}{\partial r}\right)\big|_{r=R}$ term on the right hand side.

The remaining integrals of rw are replaced with Q as per (15), and derivatives simplified using constant flow rate.

The expression for $\frac{d}{dz}\int_0^R rw^2 dr$ is very tedious, and MAPLE [37] was used for the calculation. The explicit expression is given in Appendix C of ([29]) for constant viscosity. Since the viscosity here is a function of z, there will be additional contributions from this term in the differential equation here. These extra terms are labeled α_1-α_3 in the next section, and most importantly, these terms give rise to cubic terms for the pressure gradient. Also worth noting is that all other expressions/relationships from this section are identical to [29], since all expressions in the derivation involve r, and μ only depends on z.

3.3   Differential equation for pressure

Substituting Section 3.2 results in (16) leads to a second-order non-linear ODE for the pressure gradient in the form

$$\Omega_1 \left(\frac{R^3}{\mu \overline{W}} \frac{d^2 P}{dz^2} \right) + \alpha_1 \left(\frac{R^2}{\mu \overline{W}} \frac{dP}{dz} \right)^3 + (\Omega_2 + \alpha_2) \left(\frac{R^2}{\mu \overline{W}} \frac{dP}{dz} \right)^2$$

$$+ (\Omega_3 + \alpha_3) \left(\frac{R^2}{\mu \overline{W}} \frac{dP}{dz} \right) + \Omega_4 \; = \; 0, \tag{25}$$

where all Ω_i and α_i coefficients are functions of ρ (and hence of P) and also of z, with additional linear $\frac{dP}{dz}$ dependence in Ω_1.

The Ω_i coefficients here have two extra terms compared to the coefficients in ([29]), namely the A-dependent terms in Ω_2 and in Ω_3. Furthermore, there are additional α_1-α_3 terms that arise as a result of the density-dependence in the viscosity μ, most notably introducing a cubic pressure gradient term. Finally, since μ is a function of density/pressure rather than a constant value, all Ω_i and α_i depend on A through the Reynolds number Re (see equation (33)).

The explicit expressions for the Ω_i are

$$\Omega_1 \;=\; \frac{61}{1580712} Re \frac{R^2}{\mu \overline{W}} \frac{dP}{dz} + \frac{2}{3} \frac{Ma^2}{Re} - \frac{899}{395178} \frac{w_s Re}{\overline{W}} \frac{1}{\sqrt{1 + R'^2}}$$

$$- \frac{95}{790356} \frac{w_s Re}{\overline{W}} + \frac{631}{263452} Re - \frac{61}{1580712} \frac{gR}{\overline{W}^2} Re^2 \quad (26)$$

$$\Omega_2 \;=\; -\frac{4}{3} \frac{Ma^4}{Re^2} + \frac{61}{526904} R' Re - \frac{631}{263452} Ma^2 - \frac{61}{1580712} \frac{Rg}{\overline{W}^2} Ma^2 Re$$

$$+ \frac{2}{3} A \frac{\mu_0}{\mu} \frac{\rho}{\rho_0} \frac{Ma^4}{Re^2} \tag{27}$$

$$\Omega_3 \;=\; \frac{75}{194} - \frac{1}{3} \frac{w_s}{\overline{W}} \frac{R' Ma^2}{Re \sqrt{1 + R'^2}} - \frac{95}{197589} \frac{w_s R' Re}{\overline{W}} - \frac{1798}{197589} \frac{w_s R' Re}{\overline{W} \sqrt{1 + R'^2}}$$

$$+\frac{899}{395178}\frac{w_s RR'R''Re}{\overline{W}\left(1+R'^2\right)^{3/2}}+\frac{631}{131726}R'Re-\frac{61}{263452}\frac{R'Re^2gR}{\overline{W}^2}\quad(28)$$

$$+\frac{5125}{790356}\frac{w_s}{\overline{W}}Ma^2+\frac{61}{1580712}\frac{g^2R^2}{\overline{W}^4}Ma^2Re^2+\frac{95}{790356}\frac{w_sRgMa^2Re}{\overline{W}^3}$$

$$+\frac{154937}{790356}\frac{w_s}{\overline{W}\sqrt{1+R'^2}}Ma^2+\frac{899}{395178}\frac{w_sRgMa^2Re}{\overline{W}^3\sqrt{1+R'^2}}-\frac{6610}{9409}Ma^2$$

$$+2A\frac{R'}{\sqrt{1+R'^2}}\frac{w_s}{\overline{W}}\frac{\mu_0}{\mu}\frac{\rho}{\rho_0}\frac{Ma^2}{Re}$$

$$\Omega_4\quad=\quad-\frac{75}{194}\frac{gRRe}{\overline{W}^2}+\frac{R''Rw_s}{\sqrt{1+R'^2}\,\overline{W}}+\frac{R'^2w_s}{\sqrt{1+R'^2}\,\overline{W}}+\frac{300}{97}+\frac{12}{97}\frac{w_s}{\overline{W}}$$

$$-\frac{312}{97}\frac{w_s}{\overline{W}}\frac{1}{\sqrt{1+R'^2}}+\frac{154937}{790356}\frac{R'R''w_sRRe}{\left(1+R'^2\right)^{3/2}\overline{W}}-\frac{2R''R'^2w_sR}{\left(1+R'^2\right)^{3/2}\overline{W}}$$

$$-\frac{611627}{1975890}\frac{R'w_s^2Re}{\overline{W}^2(1+R'^2)}-\frac{188159}{987945}\frac{RR'R''w_s^2Re}{\overline{W}^2(1+R'^2)^2}$$

$$-\frac{899}{395178}\frac{gRw_s}{\overline{W}^3}\frac{RR'R''Re^2}{(1+R'^2)^{3/2}}+\frac{61}{526904}\frac{R'g^2R^2Re^3}{\overline{W}^4}\quad(29)$$

$$+\frac{149}{329315}\frac{R'R''w_s^2RRe}{\left(1+R'^2\right)\overline{W}^2}-\frac{149}{329315}\frac{RR'^3R''w_s^2Re}{\overline{W}^2(1+R'^2)^2}$$

$$-\frac{23837}{3951780}\frac{R'R''w_s^2RRe}{\left(1+R'^2\right)^{3/2}\overline{W}^2}-\frac{631}{131726}\frac{R'gRRe^2}{\overline{W}^2}-\frac{6610}{9409}R'Re$$

$$+\frac{23837}{1975890}\frac{R'w_s^2Re}{\sqrt{1+R'^2}\,\overline{W}^2}+\frac{1798}{197589}\frac{R'gRw_sRe^2}{\sqrt{1+R'^2}\,\overline{W}^3}$$

$$+\frac{149}{329315}\frac{R'^3w_s^2Re}{(1+R'^2)\overline{W}^2}+\frac{95}{197589}\frac{R'gRw_sRe^2}{\overline{W}^3}$$

The explicit expressions for the α_i are

$$\alpha_1\quad=\quad-\frac{1}{2}A\frac{\mu_0}{\mu}\frac{\rho}{\rho_0}\frac{61}{790356}Ma^2\quad(30)$$

$$\alpha_2\quad=\quad\frac{1}{2}A\frac{\mu_0}{\mu}\frac{\rho}{\rho_0}\left(\frac{61}{395178}\frac{gRMa^2Re}{\overline{W}^2}+\frac{899}{197589}\frac{w_sMa^2}{\overline{W}\sqrt{1+R'^2}}\right.$$
$$\left.-\frac{631}{131726}Ma^2+\frac{95}{395178}\frac{w_sMa^2}{\overline{W}}\right)\quad(31)$$

$$\alpha_3\quad=\quad\frac{1}{2}A\frac{\mu_0}{\mu}\frac{\rho}{\rho_0}\left(-\frac{899}{197589}\frac{gRw_sMa^2Re}{\overline{W}^3\sqrt{1+R'^2}}-\frac{61}{790356}\frac{g^2R^2Ma^2Re^2}{\overline{W}^4}\right.$$

$$+\frac{631}{131726}\frac{gRMa^2Re}{\overline{W}^2}-\frac{95}{395178}\frac{gRw_sMa^2Re}{\overline{W}^3}\Bigg) \tag{32}$$

The generalized Reynolds (Re) and Mach (Ma) numbers in these expressions are defined as

$$Re \;=\; \frac{\rho\overline{W}R}{\mu}, \quad Ma \;=\; \frac{\overline{W}}{\sqrt{\frac{k_BT}{m}}}, \tag{33}$$

where again, the viscosity μ here depends on the pressure/density.

4   Parameter relationships and flow geometries

4.1   Upstream properties

The differential equation for the pressure in the previous section depends on generalized, or rather z-dependent, dimensionless numbers. In order to solve the differential equation, one has to rewrite everything in terms of constant upstream variables whose values can then be specified. This can be achieved by using the constant flow rate relationship (15), which essentially means

$$\rho_0 R_0^2 \overline{W}_0 \;=\; \rho R^2 \overline{W}. \tag{34}$$

Noting that the upstream Reynolds number Re_0 satisfies $Re_0 \;=\; Re|_{\rho=\rho_0} = \frac{\rho_0\overline{W}_0 R_0}{\mu_0(1+A)}$, it follows that

$$Re \;=\; \frac{R_0}{R}\frac{1+A}{1+A\frac{\rho}{\rho_0}}Re_0 \tag{35}$$

$$Ma \;=\; \frac{\rho_0 R_0^2}{\rho R^2}Ma_0 \tag{36}$$

$$\frac{w_s}{\overline{W}} \;=\; \frac{\rho R^2}{\rho_0 R_0^2}\frac{w_s}{\overline{W}_0} \tag{37}$$

$$\frac{Rg}{\overline{W}^2} \;=\; \left(\frac{\rho}{\rho_0}\right)^2\left(\frac{R}{R_0}\right)^5\frac{R_0 g}{\overline{W}_0^2} \tag{38}$$

where Re_0 and Ma_0 are the constant upstream Reynolds and Mach numbers respectively, and $\overline{W}_0$ is the average velocity upstream. Note that the upstream viscosity is $\mu|_{\rho=\rho_0} = \mu_0(1+A)$ rather than μ_0.

Additionally, solving (9) upstream where $\frac{dP}{dz} = 0$, $\rho = \rho_0$ is constant, $u = 0$, $w = w(r)$,and $\mu = \mu_0(1+A)$ is constant, the r-dependent axial velocity is found to be

$$w(r) \;=\; \frac{\rho_0 g}{4\mu_0(1+A)}(R_0^2 - r^2) + w_s, \tag{39}$$

where $w(r = R_0) = w_s$ is imposed together with $w(r = 0)$ being finite.

Thus upstream, the centerline velocity is

$$W_0 \;\; = \;\; w(r=0) \;\; = \;\; \frac{\rho_0 g R_0^2}{4\mu_0(1+A)} + w_s, \tag{40}$$

while the average upstream velocity is

$$\overline{W}_0 \;\; = \;\; \frac{\int_0^{R_0} rw\ dr}{\int_0^{R_0} r\ dr} \;\; = \;\; \frac{\rho_0 g R_0^2}{8\mu_0(1+A)} + w_s. \tag{41}$$

Note that this is implies $2(\overline{W}_0 - w_s) = W_0 - w_s \Rightarrow W_0 = 2\overline{W}_0 - w_s$, as consistent with (24) upstream.

Dividing (41) by $\overline{W}_0$ gives

$$1 = \frac{1}{8}\frac{\rho_0 \overline{W}_0 R_0}{\mu_0(1+A)}\frac{g R_0}{\overline{W}_0^2} + \frac{w_s}{\overline{W}_0} \quad \Rightarrow \quad 1 = \frac{1}{8}Re_0\frac{g R_0}{\overline{W}_0^2} + \frac{w_s}{\overline{W}_0} \tag{42}$$

$$\Rightarrow \quad Re_0 = \frac{8(1-w_s^0)}{g^0}, \tag{43}$$

where $w_s^0 = \frac{w_s}{\overline{W}_0}$ and $g^0 = \frac{g R_0}{\overline{W}_0^2}$ are dimensionless wall slip and forcing terms respectively scaled by (constant) upstream quantities.

4.2   Flow Geometries

In order to discuss the effects of compressibility and slip for physiologically relevant flows, as well as for numerical results from particle-based simulations, two different flow geometries will be discussed. The following axisymmetric geometries described by $R = R(z)$ will be considered:

(i) $R(z) = R_0(1 - \delta e^{-lz^2})$ (Gaussian geometry)

(ii) $R(z) = \begin{cases} R_0 & z \le z_1 \\ az^3 + bz^2 + cz + d & z_1 \le z \le z_1 + l_1 \\ ez^3 + fz^2 + gz + h & z_1 + l_1 \le z \le z_1 + l_1 + l_2 \\ R_0 & z \ge z_3 \end{cases}$ (44)

(asymmetric polynomial geometry)

In both cases, δ controls the severity of the constriction, and l or $l_1 + l_2$ controls the length of the constriction. The center of the symmetric constriction in (i) is at $z = 0$, while (ii) is asymmetric with maximum constriction at $z_1 + l_1$. Explicit expressions for a to h can be found in [16, 38, 29].

Flow geometry (i) is relevant for blood flow applications in large vessels [28, 38, 29], while (ii) has been used in particle-based flow simulations [16, 38, 21].

5   Results

The pressure differential equation from Section 3 is solved numerically.

The second-order non-linear differential equation for pressure, equation (25), can be written as the first-order system for density (using the equation of state)

$$\frac{dx}{dz} = y \tag{45}$$

$$\frac{dy}{dz} = -\frac{\alpha_1 a^3 y^3 + (\Omega_2 + \alpha_2)a^2 y^2 + (\Omega_3 + \alpha_3)ay + \Omega_4}{(\tilde{\Omega}_1 + \frac{61}{1580712} Re\ ay)aR}$$

where $x = \rho$, $y = \frac{d\rho}{dz}$, $a = \frac{R^2}{\mu \overline{W}}$, $\tilde{\Omega}_1$ is Ω_1 without the $\frac{dP}{dz}$ term, and z is the axial coordinate of the cylinder. Using Matlab [39], this system is solved numerically using the fourth-order Runge-Kutta method, and results are presented for both large vessels (flow geometry (i) with large Reynolds and small Mach numbers), and small vessels (flow geometry (ii) with small Reynolds and large Mach numbers).

5.1   Large Vessels

Following [28, 38, 29], numerical solutions are obtained for the Gaussian flow geometry (i) with fixed parameter values

$$\rho_0 = 1050 \text{ kg/m}^3, \ \mu_0 = 0.0035 \text{ kg/ms}, \tag{46}$$
$$\delta = 0.1, \ l = 2500 \text{ m}^{-2}, \ R_0 = 0.01 \text{ m}$$

Numerical solutions are presented to assess the affect of Reynolds number, compressibility, slip and viscosity/density parameter. As such, values for Re_0, Ma_0, w_{s0} and A are specified first.

In order for the first-order system (45) to have an equilibrium point at $(\rho_0, 0)$, with upstream properties discussed in Section 4.1, g_0, $\overline{W}_0$ and $\frac{k_B T}{m}$ are then determined from

$$g_0 = \frac{8}{Re_0}(1 - w_{s0}), \quad \overline{W}_0 = \frac{Re_0 \mu_0 (1 + A)}{\rho_0 R_0}, \quad \frac{k_B T}{m} = \frac{\overline{W}_0^2}{Ma_0^2}. \tag{47}$$

The effect of varying A is considered in Figures 1 to 3, where deviations from the $A = 0$ curves are also shown since deviations are small in all cases. Figure 1 shows the scaled pressure curve for $A = 0$, and deviations from this curve for different values for A. It can be seen that the pressure deviation from the $A = 0$ curve is small and negative, and increases in magnitude downstream of the constrictions as A increases, indicating a pressure reduction for larger values of A compared to the $A = 0$ curve. The pressure gradient deviations (Figure 2) are also small, and likewise increase in magnitude for larger values of A. The scaled centerline velocity deviation shown in Figure 3
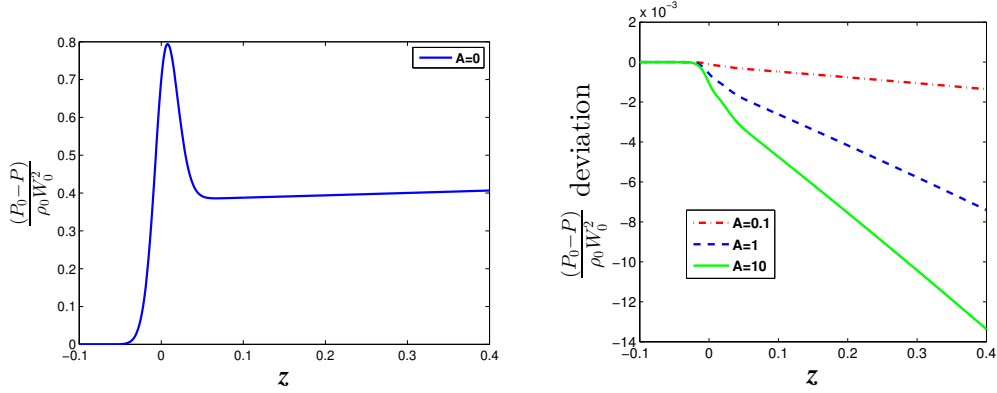
Figure 1: Scaled pressure for $A = 0$ (left) and deviation of scaled pressure from the $A = 0$ pressure curve (right) ($Re_0 = 100$, $Ma_0 = 0.1$, $w_{s0} = 0.05$)

indicates slower centerline velocities for larger values of A in the converging portions of the constriction, faster centerline velocities in the diverging portion, and smaller post-constriction centerline velocities than the $A = 0$ curves as A increases.

Although there are some changes in the nature of the solution curves as the Reynolds number increases (see the $Re_0 = 700$ curves in Figures 4 to 6) deviations are still so small that scaled pressure/pressure-gradient/centerline velocity curves are indistinguishable from the $A = 0$ curves presented in [29]. Likewise, increasing the slip and compressibility (w_{s0} and Ma_0 respectively) for the range of values considered in [29] leads to small deviations in the pressure, pressure-gradient and centerline velocity curves as A is increased to 10 (not shown). It is also worth noting that the scaled pressure deviation and the scaled pressure gradient deviation are an order of magnitude smaller in the $Re = 700$ curves compared to the $Re = 100$ curves, but that the scaled centerline velocity deviation is of the same order of magnitude in both cases.

5.2   Small vessels - multiparticle collision (MPC) flow

It was shown in [22], that multiparticle collision (MPC) flow can be interpreted as compressible flow with negligible bulk viscosity, and

$$\mu^{MPC} \quad \approx \quad \mu^{MPC}_{approx} \;=\; \mu_0 \left(1 + A \frac{\rho}{\rho_0} \right), \tag{48}$$

where

$$\mu_0 \;=\; \frac{m}{(\Delta x)^3} \left[\frac{k_B T}{2m} \Delta t \frac{5}{2 - \cos\alpha - \cos 2\alpha} - \frac{(\Delta x)^2}{18\Delta t} (1 - \cos\alpha) \right], \tag{49}$$
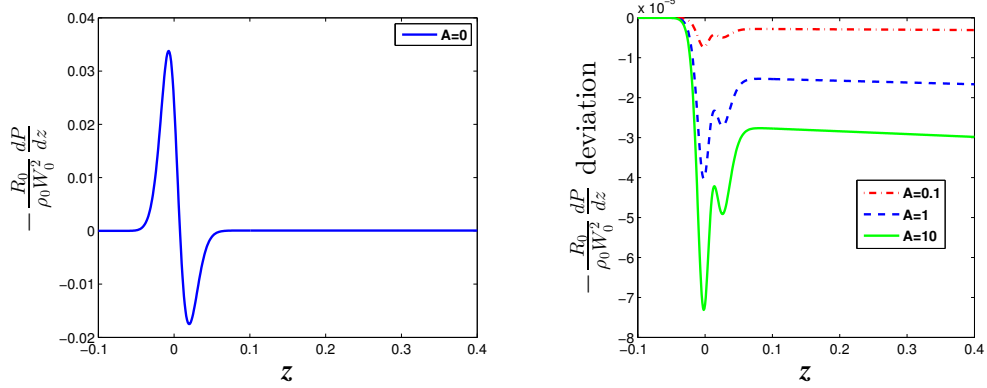
Figure 2: Scaled pressure gradient for $A = 0$ (left) and deviation of scaled pressure gradient from the $A = 0$ pressure gradient curve (right) ($Re_0 = 100$, $Ma_0 = 0.1$, $w_{s0} = 0.05$)
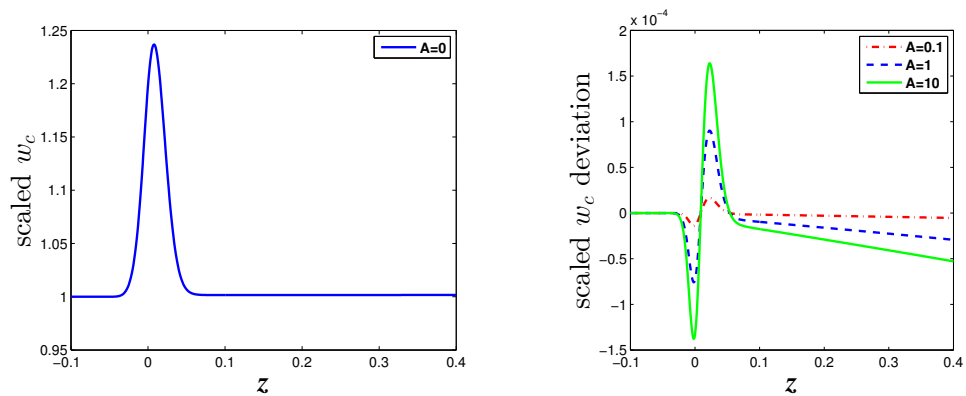

Figure 3: Scaled centerline velocity for $A = 0$ (left) and deviation of scaled centerline velocity from the $A = 0$ centerline velocity curve (right) ($Re_0 = 100$, $Ma_0 = 0.1$, $w_{s0} = 0.05$)
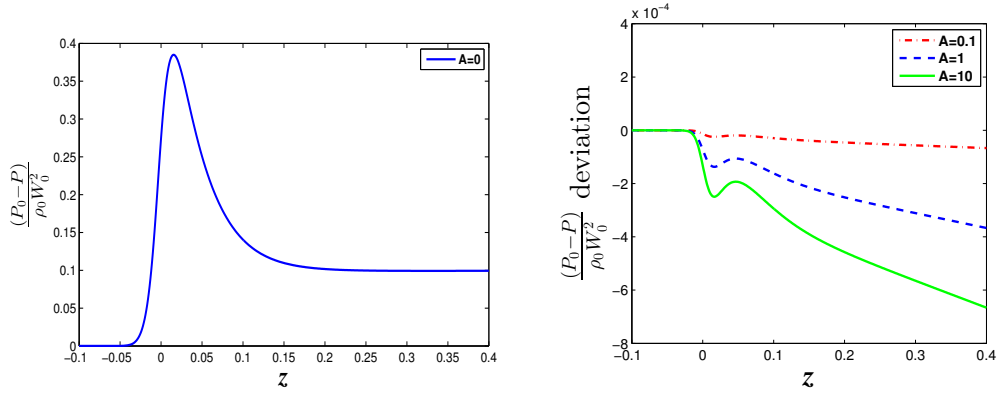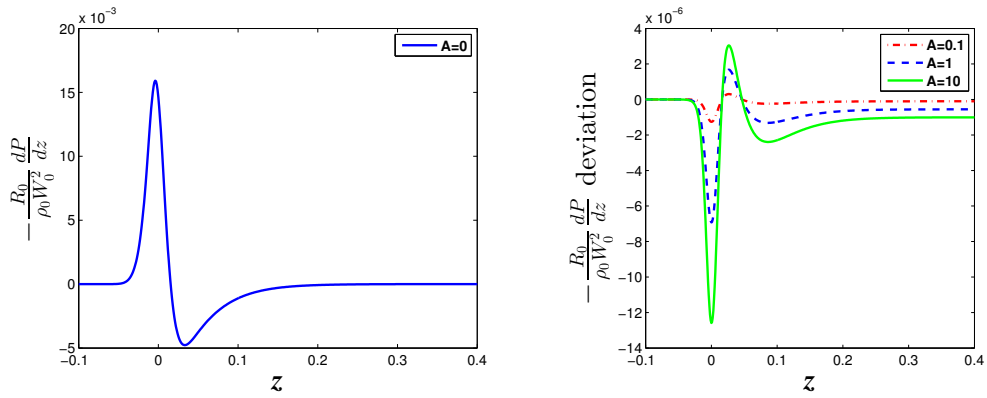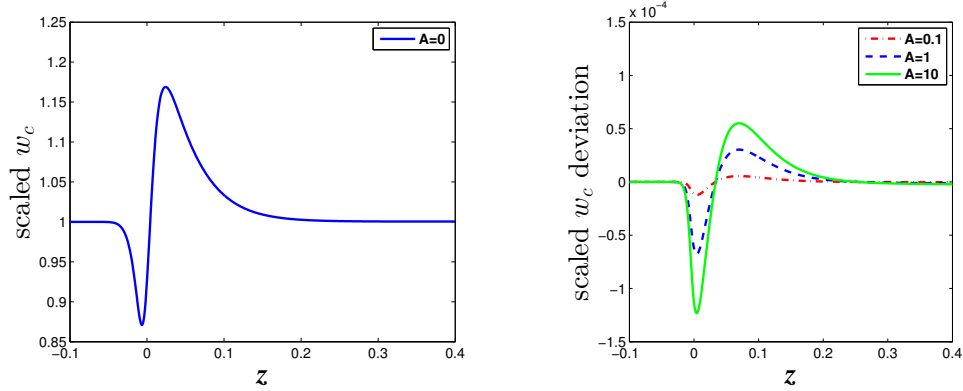
Figure 4: Scaled pressure for $A = 0$ (left) and deviation of scaled pressure from the $A = 0$ pressure curve (right) ($Re_0 = 700$, $Ma_0 = 0.1$, $w_{s0} = 0.05$)

Figure 5: Scaled pressure gradient for $A = 0$ (left) and scaled deviation of pressure gradient from the $A = 0$ pressure gradient curve (right) ($Re_0 = 700$, $Ma_0 = 0.1$, $w_{s0} = 0.05$)

Figure 6: Scaled centerline velocity for $A = 0$ (left) and deviation of scaled centerline velocity from the $A = 0$ curve (right) ($Re_0 = 700$, $Ma_0 = 0.1$, $w_{s0} = 0.05$)

and

$$A = \rho_0 \frac{\frac{k_B T}{2m} \Delta t \left(\frac{5}{2 - \cos \alpha - \cos 2\alpha} - 1 \right) + \frac{(\Delta x)^2}{18 \Delta t}(1 - \cos \alpha)}{\mu_0}. \tag{50}$$

Solution curves from (45) are compared to (dimensionless) simulation results from [21] for force-driven MPC flow through a constricted geometry given by (ii). In [21], a local thermostat is used to keep the system at constant temperature, while previous MPC flows used global thermostats [16, 17], the latter having recently been suggested to potentially lead to unphysical flow interference. Simulations were done with $\Delta x = 1 = \Delta y = \Delta z$, $\Delta t = 1$, $k_B T = 1$, $m = 1$, $R_0 = 10.5$ and $\alpha = \pm \pi/2$ (random rotation angle), so that the μ_0 and A values for the simulations correspond to

$$\mu_0 = \frac{7}{9}, \ A = \frac{1}{2}\rho_0. \tag{51}$$

Different values for g were used in the simulations, as well as different severities of the constriction δ. Data from the simulation results was used to determine values for W_0, w_s, and ρ_0.

In order for $(x, y) = (\rho_0, 0)$ to be an equilibrium solution of (45), instead of using the A value from (51), the A value was instead specified from equation (41), namely

$$A = \frac{g_0 \rho_0 \overline{W}_0 R_0}{8(1 - w_{s0})\mu_0} - 1 \tag{52}$$

In all of these equations, ρ_0 is the upstream density obtained from numerical simulations.

g	δ	λ	ρ_0	w_s	W_0	A (52)	A (51)
0.005	0.5	0	19.9637	0	0.310190	10.4037	9.98185
0.005	0.5	0.5	19.7949	0.0325045	.351665	9.9895	9.89745
0.005	1	0	19.9233	0	0.309775	10.3959	9.96165
0.005	1	0.5	19.7548	0.0317225	0.351492	9.9464	9.8774
0.01	0.5	0	19.9509	0	0.620233	10.3991	9.97545
0.01	0.5	0.5	19.7862	0.0639938	0.703284	9.9680	9.8931

Table 1: MPC data used for analytical solution. $\overline{W}_0$ is found from $0.5(W_0 + w_s)$.

Parameter values used to determine the analytical solution through the constricted portion are summarized in Table 1. For comparison, the value for A from (51) is included in the Table, although the value for A from (52) is used to obtain the analytical solutions.

Since MPC simulations lead to an increase in density upstream of the constriction, which is not something the analytical model can capture, the MPC density value at the start of the constriction at $z = 600.5$ is used as the initial density for the second-order non-linear ODE, together with zero initial derivative of the density. The ODE is solved through the constricted portion (from $z = 600.5$ to $z = 630.5$) and thereafter. Results are shown in Figures 7 to 12.

In the constrictions with the smallest Reynolds and Mach numbers ($g = 0.005$), there is fairly good agreement in the mildest ($\delta = 0.5$, Figs. 7 and 8) and more severe ($\delta = 1$, Figs. 9 and 10) constrictions considered, for both slip (Fig. 8 and 10) and no-slip (Fig. 7 and 9) conditions. The scaled centerline densities seem to be slightly overestimated by the theory in the case of no slip (left graphs in Fig. 7 and 9), while underestimates are seen in the slip cases (left graphs in Fig. 8 and 10). In all cases, the scaled centerline velocity peak is overestimated by the theoretical curves, and settles to the post-constriction equilibrium values much sooner than the MPC simulation results. The post-constriction equilibria are well estimated by the theoretical results, however they are slightly smaller compared to MPC results in the case of slip (right graphs in Fig. 8 and 10).

Increasing the flow speed ($g = 0.1$), that subsequently also increases compressibility/Mach numbers, leads to a larger discrepancy between the analytical and the numerical results (see Fig. 11 and 12), although better agreement in density for the slip case (Fig. 12), compared to better agreement for centerline velocity in the no-slip (Fig. 11) case.

Increasing flow speeds further to $g = 0.2$, agreement worsens (not shown), and solutions diverge for large enough slip (not shown).
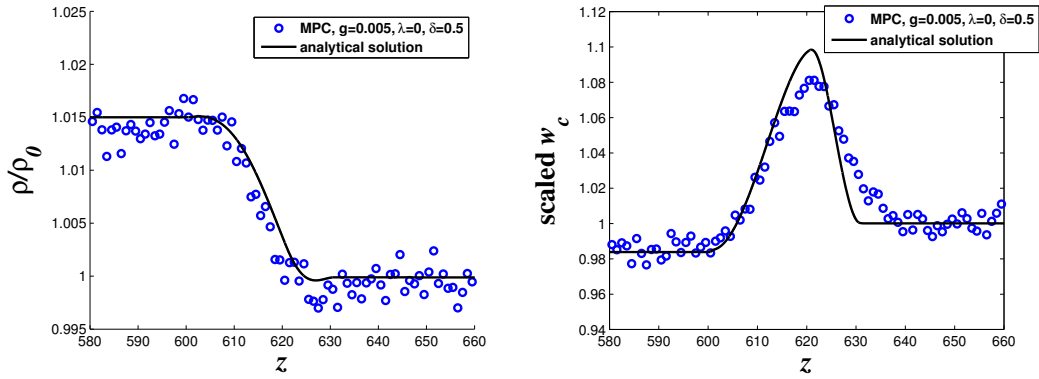
Figure 7: Scaled centerline density (left) and scaled centerline velocity (right) for MPC flow (no slip).
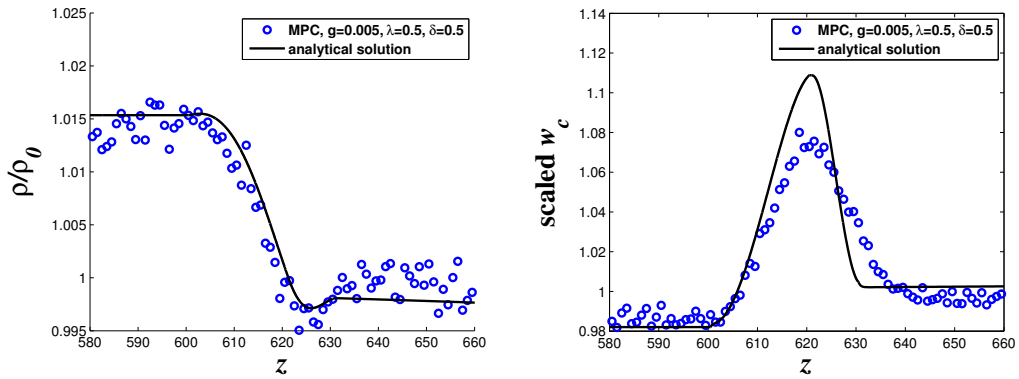

Figure 8: Scaled centerline density (left) and scaled centerline velocity (right) for MPC flow (slip).
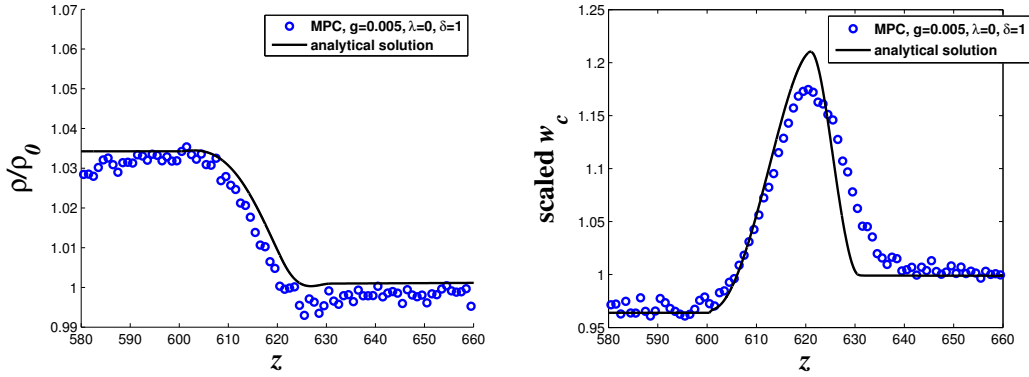
Figure 9: Scaled centerline density (left) and scaled centerline velocity (right) for MPC flow (no slip).
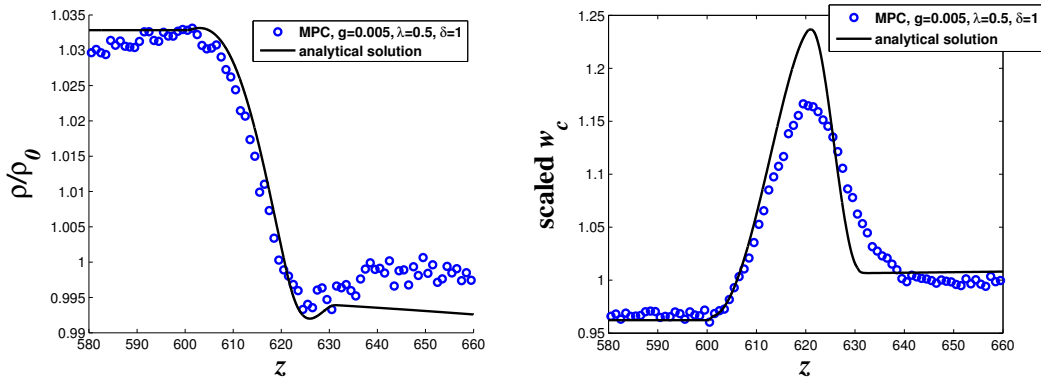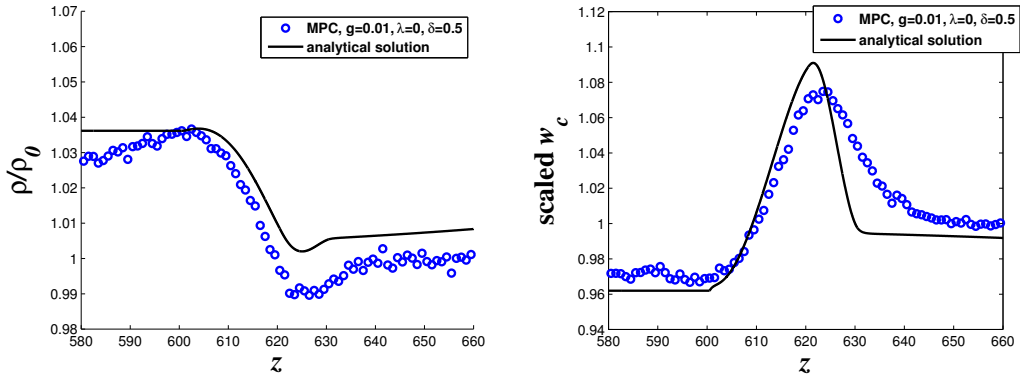

Figure 10: Scaled centerline density (left) and scaled centerline velocity (right) for MPC flow (slip).

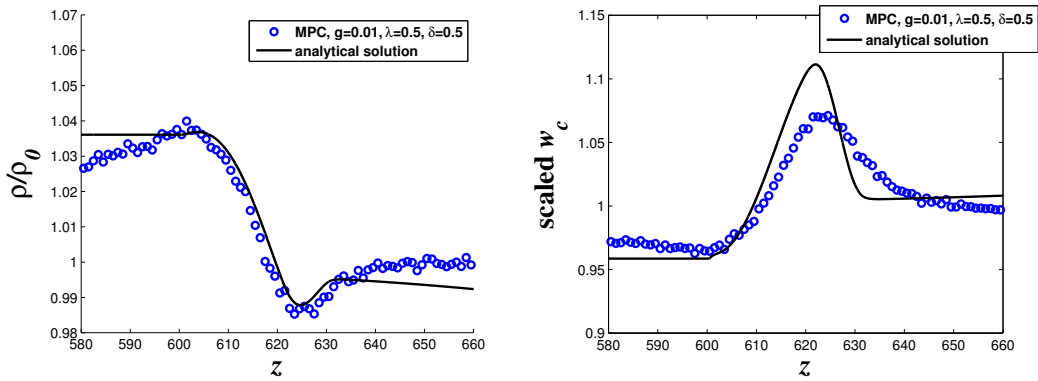Figure 11: Scaled centerline density (left) and scaled centerline velocity (right) for MPC flow (no slip).

Figure 12: Scaled centerline density (left) and scaled centerline velocity (right) for MPC flow (slip).

6 Discussion

In the large vessels considered, only very small changes are found for $A \in [0, 10]$ for the scaled variables of interest. It is worth pointing out that the Figures in this paper show scaled pressure gradient curves (Fig. 2 and 5), while in the literature the dimensionful pressure gradient is typically presented (see [28, 29]). If the dimensionful pressure gradient was plotted here, its value would change drastically as A increases since the pressure gradient scaling factor $\frac{R_0}{\rho_0 W_0^2} = \frac{R_0}{\rho_0 (2\overline{W}_0 - w_s)^2}$, and $\overline{W}_0$ is proportional to $(1 + A)$ according to (47). So, if $A = 10$, this scaling factor gives a dimensionful pressure gradient that is approximately two orders of magnitude larger than its $A = 0$ counterpart for the same Re_0.

In the small vessels considered, the analytical solution was compared to multiparticle collision dynamics (MPC) simulation results. Agreement was fairly good, however, far enough downstream of the constriction, the solution eventually lead to either larger and larger values for ρ, or smaller and smaller values (results not shown). This divergence of the solution can be explained by looking at the phase-plane diagram. The non-linear system (45) can be shown to have two equilibrium points

$$(\rho_0, 0), \quad \text{and} \quad \left(-\frac{\rho_0}{A + 1 - w_{s0}}, 0 \right).$$

For small enough slip, $w_{s0} < 1$, and thus only the first equilibrium point is a physically meaningful equilibrium.

Using Maple [37], the derivative matrix evaluated at the physically meaningful equilibrium point $(\rho_0, 0)$ is

$$\mathbf{M} = \begin{bmatrix} 0 & 1 \\ \frac{25200\mu_0^2 Re_0^2 (A^2 - Aw_{s0} + 3A + 2 - w_{s0})}{\rho_0^2 (5432 Ma_0^2 + 17Re_0^2 - 17Re_0^2 w_{s0}) R_0^4} & m \end{bmatrix}$$

where

$$m = \frac{-2Re_0 [1575(A + 1) + Ma_0^2 (-2784A + 747w_{s0}A - 2852 - 68w_{s0}^2 + 883w_{s0})]}{(5432 Ma_0^2 A + 17Re_0^2 A - 17Re_0^2 w_{s0}A + 5432 Ma_0^2 + 17Re_0^2 - 17Re_0^2 w_{s0}) R_0}$$

Since

$$\det \mathbf{M} = -\frac{25200\mu_0^2 Re_0^2 (A^2 - Aw_{s0} + 3A + 2 - w_{s0})}{\rho_0^2 (5432 Ma_0^2 + 17Re_0^2 - 17Re_0^2 w_{s0}) R_0^4}$$

and $w_{s0} < 1$, it follows that $\det \mathbf{M} < 0$. Thus, $(\rho_0, 0)$ is a saddle point. This is true for vessels of any size, although this divergence in the solution was not observed in the large vessel solution curves from Section 5.1. To further shed light on this apparent discrepancy, typical phase portraits for large vessels (Fig. 13) and for MPC flows (Fig. 14) reveal a stable manifold ($dy/dz = 0$ solid line) near $(\rho_0, 0)$ in large vessels (Fig. 13). At the end of the
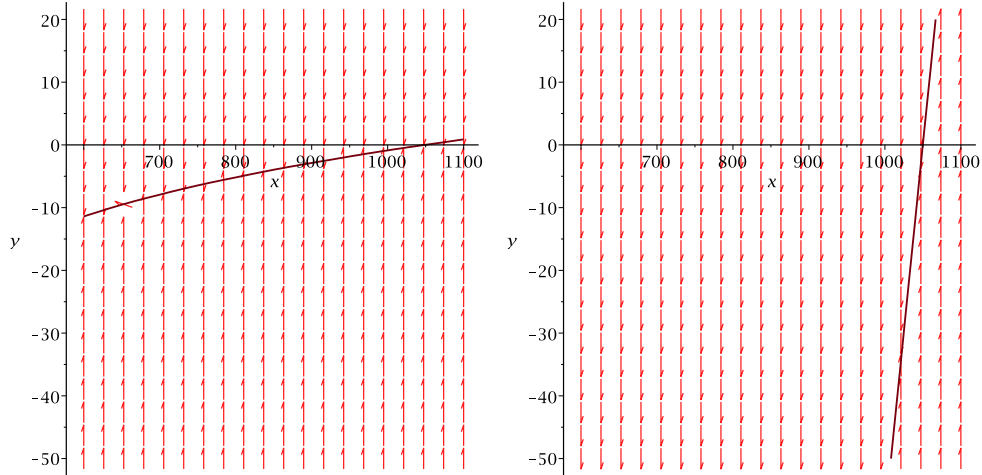
Figure 13: Phase Portraits for $x = \rho$, $y = \frac{d\rho}{dz}$ in large vessels for $A = 0$ (left) and $A = 10$ (right), together with the $dy/dz = 0$ curve (solid line). In both cases, $w_{s0} = 0.05$, $Re_0 = 100$, and $Ma_0 = 0.1$, $R_0 = 0.01\ m$, $\delta = 0$, $\rho_0 = 1050\ kg/m^3$.

constricted portion, the pressure gradient is typically positive, and density is smaller than ρ_0 (see Section 4 figures). The near vertical arrows indicate that the pressure/density solution will then have constant ρ_0 for some time (Fig. 13), until the solid line is reached, and then solutions will travel to the left following the solid line. In Fig. 13, this leads to at most, small decreases in ρ in the post-constriction region, however, if the simulations were done for longer vessels, the solution would also diverge there eventually. In Figure 14 for the MPC phase portraits, the solid line has a different role as it is no longer a stable manifold and decreases in density are much more pronounced especially for larger values of g (phase portrait on the right). Since larger values for g lead to larger Mach numbers, compressibility is likely too large for the theory to be valid.
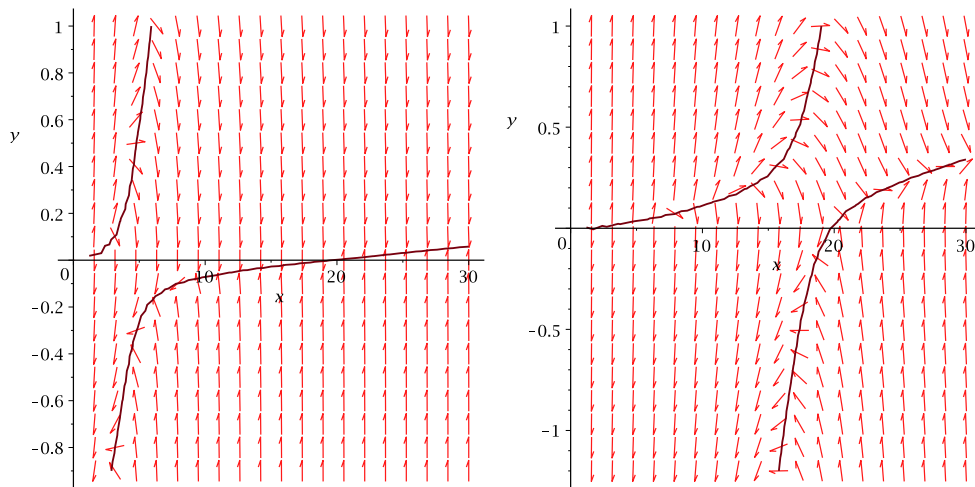
Figure 14: Phase Portraits for $x = \rho$, $y = \frac{d\rho}{dz}$ for MPC simulation for $g = 0.005$ (left) and $g = 0.02$ (right), together with the $dy/dz = 0$ curve (solid line). In both cases, $\lambda = 0.2$.

7   Summary and Conclusions

A second-order non-linear differential equation for pressure/density is derived for a weakly compressible fluid, with density-dependent viscosity and slip, through a local constriction. Solution curves are presented for pressure/density curves, for the pressure/density gradient, and for the centerline velocity. The effect of the viscosity-density parameter A is explored for large vessels (section 5.1) where compressibility and slip values are taken to be relatively small, and for small vessels (section 5.2) with larger compressibility and slip. The former has application to blood flow studies, while the latter can be applied to microfluidics and particle-based flow simulations.

Solution curves for scaled pressure, scaled pressure gradient, and scaled centerline velocity were found to be fairly insensitive to changes in A for the range $[0, 10]$ in the large vessels considered. For the smaller vessels, scaled centerline densities agreed well with particle-based simulations for mild constrictions with small Reynolds/Mach numbers. Solutions to the ODE for the pressure were found to eventually lead to $\rho \to 0$ in the post-constriction region, and this was much more pronounced in the smaller vessels with large Reynolds/Mach numbers. This was explained by means of a phase-plane analysis of the equivalent first-order system.

The implications of this study are as follows: Negative pressures ($P_0 - P < 0$) have been connected to possibly lead to further development of plaques in blood flow applications [28]. In the study here, neither compressibility, slip or viscosity-density dependence would give rise to such pressures for the (physiologically meaningful) Reynolds numbers considered here. However, particle-based flow studies show that negative pressures can be captured by the model, and the model can still be used to predict density variations even when the compressibility is high. Assumptions corresponding to particle-based method simulation models in complex flow domains may not be clear a priori, and analytical models — such as the one presented here — would be useful to gain insight into the dynamics.

8   Acknowledgements

References

[1] S.S. Varghese, S.H. Frankel, and P.F. Fischer. Direct numerical simulation of stenotic flows. Part 1. Steady flow. *J. Fluid Mech.*, 582:253–280, 2007.

[2] S.A. Berger and L-D. Jou. Flows in stenotic vessels. *Annu. Rev. Fluid Mech.*, 32:347–382, 2000.

[3] S.A. Berger, J.S. Stroud, and D. Saloner. Influence of stenosis morphology through severely stenotic vessels: implications for plaque rupture. *J. Biomechan.*, 33:443–455, 2000.

[4] W. Liao, T. S. Lee, and H. T. Low. Numerical studies of physiological pulsatile flow through constricted tube. *Internat. J. Numer. Methods Heat Fluid Flow*, 14:689–713, 2004.

[5] J. H. Forrester and D. F. Young. Flow through a converging-diverging tube and its implications in occlusive vascular disease I: Theoretical development. *J. Biomechan.*, 3:297–385, 1970.

[6] J.C. Misra and G.C. Shit. Role of slip velocity in blood flow through stenosed arteries: A non-Newtonian model. *J. Mech. Med. Biol.*, 7:337–353, 2007.

[7] G. Pontrelli. Blood flow through an axisymmetric stenosis. *Proc. Instn. Mech. Engrs. Part H*, 215:1–10, 2001.

[8] H. Huang, V.J. Modi, and B.R. Seymour. Fluid mechanics of stenosed arteries. *Internat. J. Engrg. Sci.*, 33:815–828, 1995.

[9] H.A. Stone, A.D. Stroock, and A. Ajdari. Engineering flows in small devices: Microfluidics toward a lab-on-a-chip. *Annual Review of Fluid Mechanics*, 36:381–411, 2004.

[10] W.-M. Zhang, G. Meng, and X. Wei. A review on slip models for gas microflows. *Microfluidics and Nanofluidics*, 13:845–882, 2012.

[11] C. Hong, Y. Asako, M. Faghri, and J.-H. Lee. Poiseuille number correlations for gas slip flow in microtubes. *Numerical Heat Transfer, Part A-Applications*, 56:785–806, 2009.

[12] Y. Nubar. Blood flow, slip, and viscometry. *Biophys. J.*, 11:252–264, 1971.

[13] D. Hershey and S.J. Cho. Blood flow in rigid tubes, thickness and slip velocity of plasma film at the wall. *J. Appl. Physiol.*, 21:27–32, 1966.

[14] A. Nakano, Y. Sugii, M. Minamiyama, J. Seki, and H. Niimi. Velocity profiles of pulsatile blood flow in arterioles with bifurcation and confluence in rat mesentery measured by particle image velocimetry. *JSME Int. J., Series C*, 48:444–452, 2005.

[15] C. Picart, P.H. Carpentier, H. Galliard, and J-M. Piau. Blood yield stress in systemic sclerosis. *Am. J. Physiol. Heart Circ. Physiol.*, 276:H771–H777, 1999.

[16] T. Akhter and K. Rohlf. Quantifying compressibility and slip in multiparticle collision (MPC) flow through a local constriction. *Entropy*, 16:418–442, 2014.

[17] S. Bedkihal, J. C. Kumaradas, and K. Rohlf. Steady flow through a constricted cylinder by multiparticle collision dynamics. *Biomechan. Model. Mechanobiol.*, 12:929–939, 2013.

[18] V.K. Verma, M.P. Singh, and V.K. Katiyar. Mathematical modeling of blood flow through stenosed tube. *J. Mechan. Med. Biol.*, 8:27–32, 2008.

[19] J.G. Zhou. Axisymmetric lattice Boltzmann method. *Phys. Rev. E*, 78:036701–1–7, 2008.

[20] J.R. Darias, M. Quiroga, E. Medina, P.J. Colmenares, and V.R. Paredes. Simulation of suspensions in constricted geometries by dissipative particle dynamics. *Molec. Sim.*, 29:443–449, 2003.

[21] P. Kunwar. *Shear viscosity calculation for particle-based flow, Toronto, Ontario, Canada*. M. Sc. Thesis, Department of Mathematics, Ryerson University, 2014.

[22] L. Regmi and K. Rohlf. Weakly compressible flow through a cylinder with pressure-dependent viscosity and navier-slip at the wall. *Eur. J. Mech. B/Fluids*, 60:13–23, 2016.

[23] C. LeRoux. Flow of fluids with pressure dependent viscosities in an orthogonal rheometer subject to slip boundary conditions. *Meccanica*, 44:71–83, 2009.

[24] F.J. Martinez-Boza, M.J. Martin-Alfonso, C. Gallegos, and M. Fernández. High-pressure behavior of intermediate fuel oils. *Energy & Fuels*, 25:5138–5144, 2011.

[25] K.R. Rajagopal, G. Saccomandi, and L. Vergori. Flow of fluids with pressure- and shear-dependent viscosity down an inclined plane. *Journal of Fluid Mechanics*, 706:173–189, 2012.

[26] J.M. Dealy and J. Wang. *Melt Rheology and its Applications in the Plastics Industry, 2nd edition*. Springer, 2013.

[27] J. H. Forrester and D. F. Young. Flow through a converging-diverging tube and its implications in occlusive vascular disease II: Theoretical and experimental results and their implications. *J. Biomechan.*, 3:307–316, 1970.

[28] L. Yao and D.-Z. Li. Pressure and pressure gradient in an axisymmetric rigid vessel with stenosis. *Appl. Math. Mech. (English Ed.)*, 27:347–351, 2006.

[29] S. Rabba and K. Rohlf. Pressure curves for compressible flows with slip through asymmetric local constrictions. *to appear in Int. J. Appl. Nonlinear Sci.*, 2017.

[30] R. Devanathan and S. Parvathamma. Flow of micropolar fluid through a tube with stenosis. *Med. & Biol. Eng. & Comput.*, 21:438–445, 1983.

[31] R.N. Pralhad and D.H. Schultz. Modeling of arterial stenosis and its applications to blood diseases. *Math. Biosci.*, 190:203–220, 2004.

[32] S. Nadeem, N.S. Akbar, A.A. Hendi, and T. Hayat. Power law fluid model for blood flow through a tapered artery with a stenosis. *Appl. Math. Comput.*, 217:7108–7116, 2011.

[33] R. J. Kee, M. E. Coltrin, and P. Glarborg. *Chemically reacting flow: Theory & Practice*. John Wiley & Sons, Inc., 2003.

[34] R. L. Panton. *Incompressible flow (3rd Edition)*. John Wiley & Sons, Inc., 2005.

[35] T. Ihle and D. Kroll. Stochastic rotation dynamics. II. Transport coefficients, numerics, and long-time tails. *Phys. Rev. E*, 67:066706–1–17, 2003.

[36] S. Poyiadji, K.D. Housiadas, K. Kaouri, and G.C. Georgiou. Asymptotic solutions of weakly compressible Newtonian Poiseuille flows with pressure-dependent viscosity. *European Journal of Mechanics B-Fluids*, 49:217–225, 2015.

[37] MAPLE. *Waterloo Maple Inc., Waterloo, Ontario, Canada*. 2012.

[38] S. Rabba. *Pressure curves for compressible flow with slip through constricted cylinders, Toronto, Ontario, Canada*. M. Sc. Thesis, Department of Mathematics, Ryerson University, 2014.

[39] MATLAB. *The MathWorks, Inc., Natick, Massachusetts, USA*.